UCLA

Title
Relativistic electrons generated at Earth's quasi-parallel bow shock

Authors

Liu, Terry Z
Angelopoulos, Vassilis
Lu, San

GEOPHYSICS

Relativistic electrons generated at Earth's quasi-parallel bow shock

Terry Z. Liu*, Vassilis Angelopoulos, San Lu

Plasma shocks are the primary means of accelerating electrons in planetary and astrophysical settings throughout the universe. Which category of shocks, quasi-perpendicular or quasi-parallel, accelerates electrons more efficiently is debated. Although quasi-perpendicular shocks are thought to be more efficient electron accelerators, relativistic electron energies recently observed at quasi-parallel shocks exceed theoretical expectations. Using in situ observations at Earth's bow shock, we show that such relativistic electrons are generated by the interaction between the quasi-parallel shock and a related nonlinear structure, a foreshock transient, through two betatron accelerations. Our observations show that foreshock transients, overlooked previously, can increase electron acceleration efficiency at a quasi-parallel shock by an order of magnitude. Thus, quasi-parallel shocks could be more important in generating relativistic electrons, such as cosmic ray electrons, than previously thought.

INTRODUCTION

Collisionless shocks, such as planetary bow shocks and supernova-driven shocks, are among the most important plasma accelerators in space and astrophysics (1, 2). Supernova-driven shocks (usually with a high Mach number, the ratio of flow speed to local sound speed) are known to generate cosmic rays, which comprise particles with extremely high (above billion electron volts) energies (2). Most collisionless shocks can be categorized on the basis of θ_{BN}, the angle between the magnetic field upstream of them and the local shock normal: quasi-parallel ($\theta_{BN} < 45°$) and quasi-perpendicular ($\theta_{BN} > 45°$). Astrophysical shocks, such as supernova-driven shocks, however, cannot be categorized as such because the magnetic field direction cannot yet be measured through remote sensing. Therefore, in situ observations, such as those at planetary bow shocks, could provide a hint of which category is more important in shock acceleration. Quasi-perpendicular shocks, especially with $\theta_{BN} \sim 90°$ (3), have been thought to accelerate electrons to much higher energies than quasi-parallel shocks (4). Recent in situ observations, however, found relativistic (more than 100 keV energies; $v > 0.5c$) electrons upstream of quasi-parallel bow shocks with both a high Mach number (at Saturn) (5) and a low Mach number (at Earth) (6). Such electron energy exceeds even the maximum electron energy (tens of kilo–electron volts) predicted by theory at quasi-perpendicular shocks (7).

What could account for this difference? Unlike quasi-perpendicular shocks, quasi-parallel shocks reflect particles that backstream along field lines, forming a region called the foreshock (4). Backstreaming particles in the foreshock can interact with upstream particles, forming numerous ion kinetic structures called foreshock transients (4). Recent in situ observations and simulations have suggested that these structures could play a role in quasi-parallel shock acceleration (6, 8–12). Using in situ observations at Earth's bow shock, we report that the interaction between electrons accelerated at quasi-parallel shocks and foreshock transients can explain the unexpected generation of relativistic electrons upstream of quasi-parallel bow shocks.

RESULTS

Simulations of a foreshock transient

To provide context and build intuition on electron interaction with foreshock transients, we use hybrid simulations to investigate how magnetic field lines typically evolve near a major category of foreshock transients, a foreshock bubble (Fig. 1 and movie S1) (13, 14). The simulated solar wind incorporates a planar rotational discontinuity (RD) that is initially uniform on both sides and across which the magnetic field is rotated by 40° (typical foreshock bubble generation conditions). As it approaches the bow shock, this discontinuity traps and thermalizes backstreaming foreshock ions on its upstream side, enhancing the local thermal pressure and distorting the magnetic field there. The enhanced thermal pressure expands the solar wind plasma supersonically and transports magnetic flux sunward from the hot region (Fig. 1A). The foreshock bubble forms a hot, tenuous, weak-field core as well as a sheath and a shock (Fig. 1B), both with strong magnetic fields, upstream of that core. As the foreshock bubble continues to evolve, field lines from the core pile up in the surrounding region (compression region in Fig. 1C), leaving a magnetic flux deficit behind them (expansion region in Fig. 1C). This development, which is common for foreshock transients, has been reported in simulations and observations elsewhere (13, 15).

Observations of a foreshock transient

Figure 2 presents THEMIS (Time History of Events and Macroscale Interactions during Substorms) (16) observations of a foreshock bubble (two additional observation examples are in the Supplementary Materials) showing relativistic electrons (100 to 400 keV, green and blue at ~21:58:12 UT (Universal Time) in Fig. 2F). As the foreshock bubble convects with the solar wind, a spacecraft (nearly still in Earth's rest frame) always observes a hot, tenuous core and then a foreshock bubble sheath (Fig. 2). Motivated by our simulations showing the solar wind flow diverging sunward and sideways from the center of the core, we separate the core into two regions (Fig. 2B): an expansion region in which the flow diverges (as the expansion is mainly along the foreshock bubble shock normal **n**, $\nabla \cdot \mathbf{V} \sim dV_n/dn \sim dV_x/dx > 0$, Fig. 2D) and a compression region in which the flow converges ($\nabla \cdot \mathbf{V} \sim dV_x/dx < 0$, Fig. 2D). As expected from the simulations (Fig. 1C), the field strength (Fig. 2A) and density (Fig. 2B), which are very low in the expansion region (~2 nT and 0.4 cm^{-3}, respectively), increase in the compression region (~4 nT and 1 cm^{-3}, respectively).

Department of Earth, Planetary, and Space Sciences, University of California, Los Angeles, Los Angeles, CA, USA.
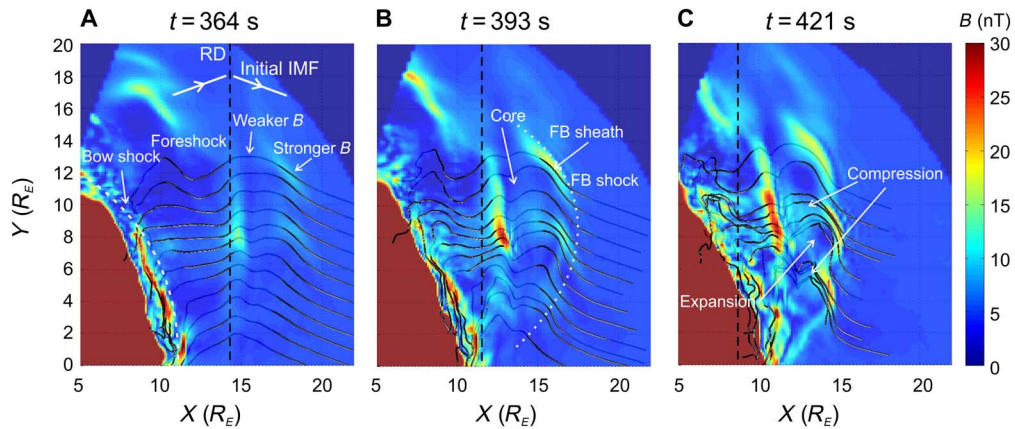*Corresponding author. Email: terryliuzixu@ucla.edu

Fig. 1. Evolution of magnetic field lines around a foreshock bubble in the GSE-*XY* plane (*z* = 0): Results of a hybrid simulation. (**A**) to (**C**) are at *t* = 364, 393, and 421 s, respectively. Colors denote field strength in nanotesla. The vertical dashed black line represents the position of the RD except when it interacts with the bow shock [indicated by the dashed white line in (A)]. The solid black lines represent solar wind magnetic field lines.
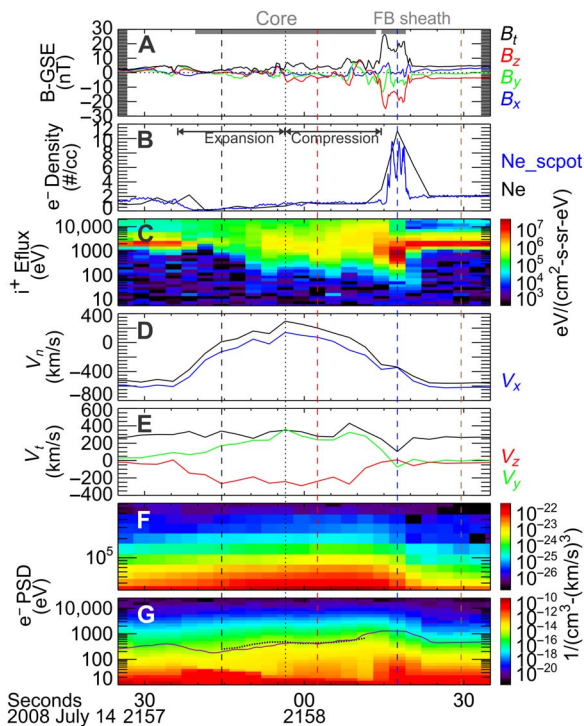

Fig. 2. THEMIS observations of a foreshock bubble. From top to bottom: (**A**) magnetic field in GSE coordinates (*X*, *Y*, *Z*, and total are in blue, green, red, and black, respectively); (**B**) electron density (e⁻ Density) from the onboard moment (black) and calculated from the high-resolution spacecraft potential (blue); (**C**) ion energy flux (i⁺ Eflux); (**D**) ion bulk velocity along the foreshock bubble shock normal V_n (n = [0.91, 0.24, −0.31] in GSE) compared with ion bulk velocity in GSE-*X* (blue); (**E**) ion bulk velocity tangential to the foreshock bubble shock normal V_t and bulk velocity in GSE-*YZ* (green and red, respectively); (**F**) electron PSD (e⁻ PSD) spectrum from 30 to 700 keV (9 s smoothed to lower noise level; for unsmoothed spectrum, see fig. S2B); (**G**) electron PSD spectrum from 10 eV to 25 keV. The solid purple line indicates the smoothed magnetic field strength scaled by a factor of 100 for comparison with the PSD spectrum contour (dotted line). The expansion region and the compression region are labeled in the core and separated by a vertical dotted line. The colored vertical dashed lines indicate the times at which electron PSD in Fig. 3 is measured.

Inside the core (demarcated by the horizontal gray bar atop Fig. 2A), the electron phase space density (PSD) contour (dotted line in Fig. 2G) and the scaled field strength (solid purple line) show very similar trends, suggesting betatron acceleration (by the electric field generated from magnetic field variations). Such trends can also be seen in Fig. 2F (hundreds of kilo–electron volts), which shows a clear rise in flux at fixed energy from the expansion region to the compression region. The energy for fixed PSD (e.g., green-yellow level) increases from ~80 to 100 keV within the expansion region to ~100 to 200 keV (relativistic energies) within the compression region. Relativistic electrons can be betatron-accelerated while piling up with field lines from the expansion region to the compression region. In addition, a plot of the electron energy for fixed PSD *E* against field strength *B* (fig. S1) shows that $E \sim B^{2/3}$ rather than $\sim B$. This is consistent with the observed magnetic fluctuations with amplitude as large as the background field inside the core (Fig. 2A), which could isotropize electrons (figs. S2 and S3, A and B), moderating the efficiency of betatron acceleration (see derivation in Materials and Methods).

In Fig. 3, we examine electron PSDs in directions perpendicular, parallel, and anti-parallel to the magnetic field in various regions (corresponding to the colored dashed vertical lines in Fig. 2). Comparing the PSD in the expansion region (black) to that in the compression region (red), we see that the PSD increase follows an energy shift by a factor of ~1.5 at energy ~ 1 keV, which is consistent with the field strength increase, ~2 ($2^{2/3} \sim 1.5$). The maximum energy of electrons detectable above instrument noise level (denoted by two black dashed lines, one for low and one for high energies, as these are measured by two instruments) also increases from ~200 to ~300 keV. Thus, the relativistic electrons observed in the compression region are indeed consistent with betatron-accelerated electrons from the expansion region.

Then, we investigate the source of energetic (several kilo–electron volts to 200 keV) electrons in the expansion region. The omnidirectional electron PSD in the expansion region (black) is nearly identical to the perpendicular PSD in the foreshock bubble sheath (blue in Fig. 3A) above 1 keV. Such similarity in PSD can also be seen in Fig. 2 (F and G) (>1 keV only). (At energies <1 keV, which make the dominant contribution to the total density, the PSD in the expansion region is much lower than that in the foreshock bubble sheath,
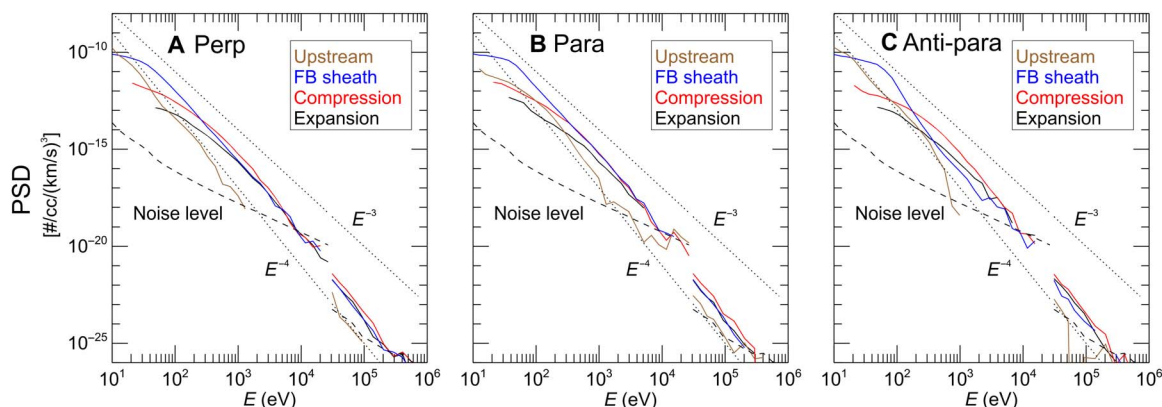
Fig. 3. Electron PSD in various regions. (A to **C)** PSD in directions perpendicular, parallel, and anti-parallel to the magnetic field, respectively. The PSD from 30 to 700 keV is smoothed over 9 s to lower the instrument noise level. The colors correspond to the colored vertical dashed lines in Fig. 2. The dotted lines indicate the slopes, −3 and −4. The dashed lines indicate the noise levels for two particle instruments.

consistent with the density ratio in the two regions, as seen in Fig. 2B.) This similarity of >1 keV electron PSDs in the expansion and sheath regions suggests that the energetic electrons in the foreshock bubble sheath could leak into the expansion region and subsequently experience betatron acceleration as discussed in the previous paragraphs. Energetic electrons can freely leak along field lines from a strong field region to a weak field region until the PSD is balanced. The cold electrons, on the other hand, cannot move freely along field lines because space-charge buildup maintains quasi-neutrality; in other words, foreshock transient dynamics are controlled by ion kinetics, and the cold electron density profile must follow the ion density profile.

Next, we examine how energetic (several kilo–electron volts to ~200 keV) electrons are generated in the foreshock bubble sheath. Comparing the perpendicular PSD (Fig. 3A) in the foreshock bubble sheath (blue) with that in the upstream background foreshock (brown), we see that their PSDs above 100 eV are well described by a factor of 2.5 energy increase. The maximum energy above the instrument noise level (dashed lines) also increases from approximately tens of kilo–electron volts to ~200 keV (Fig. 3A). This suggests that energetic electrons in the foreshock bubble sheath can be betatron-accelerated when they enter the sheath (the spin-averaged field strength at the blue line in Fig. 2A is ~17.5 nT) through the shock from the upstream background foreshock (~5 nT). The energy shift from brown to blue in Fig. 3A underestimates the energy increase ratio inferred from the field increase, likely because leakage into the expansion region lowers the PSD in the foreshock bubble sheath. Magnetic fluctuations have weaker effects here, as the background field is stronger than in the core; thus, the perpendicular anisotropy is enhanced from tens of electron volts to hundreds of kilo–electron volts, as seen in figs. S2 and S3C. In addition, the parallel PSD (Fig. 3B) above ~300 eV in the compression region (red) is nearly identical to that in the foreshock bubble sheath (blue; corresponding to the parallel flux enhancement in fig. S3C). We suggest that this is because, after they are accelerated in the compression region, energetic electrons with small enough pitch angles to be within the loss cone can leak sunward through the foreshock bubble sheath and be lost to the interplanetary medium.

The solar wind typically does not contribute notable fluxes of tens of kilo–electron volt electrons to the background foreshock. In the

upstream background foreshock (brown in Fig. 3), we see more electron flux at 1 keV to tens of kilo–electron volts in the parallel (roughly sunward) and perpendicular directions than in the anti-parallel (roughly anti-sunward) direction. Such additional electron flux suggests acceleration at the local bow shock. Moreover, we see that the electron PSDs in the foreshock transient and in the background foreshock have a similar slope, ~4 (Fig. 3). Such a slope is likely determined by the source, background foreshock electrons, as betatron acceleration with pitch-angle scattering does not affect it (only isotropizes the PSD at each energy). This further confirms that relativistic electrons originate as background foreshock electrons.

DISCUSSION

In summary, when foreshock electrons accelerated at a quasi-parallel shock enter a foreshock transient, betatron acceleration caused by crossing of the transient's shock and field-line pileup inside its core increases electron energy by up to fourfold and by two- to threefold, respectively. These processes together produce an order-of-magnitude increase in electron energies. Previous studies of the maximum energy to which electrons can be accelerated at shocks have overlooked the foreshock region and foreshock transients, which are nearly always present in planetary and astrophysical shocks but not detectable through Earth-based and space-based telescopes. This in situ study reveals that foreshock transients can increase the acceleration efficiency of quasi-parallel shocks, implying that they could play a very important role in generating galactic cosmic ray electrons. Therefore, foreshock transients should be considered as part of the shock acceleration process and viewed as extended nonlinear shock structures integral to the acceleration process in shock environments.

MATERIALS AND METHODS
Data
We used observations from NASA's THEMIS mission (*16*). In the first two dayside seasons of that mission, two THEMIS spacecraft, TH-B (~30 R_E apogee) and TH-C (~20 R_E apogee), were often in the foreshock, providing many observations of foreshock transients. We analyzed plasma data from the electrostatic analyzer (ESA; ~7 eV to 25 keV) (*17*) and the solid state telescope (SST; ~30 to 700 keV)

(16) and magnetic field data from the fluxgate magnetometer (18). Foreshock transients were selected from the event list reported in our previous statistical study (9). We chose events in particle burst mode, where ESA and SST have a higher time (3 s) and a higher angular (22.5°) resolution. We calculated the noise levels of ESA and SST using the flux of one count level multiplied by four times the SD.

Simulations

In this study, we used a three-dimensional hybrid simulation. In this code (19), electrons are described by fluid equations, and ions are advanced by the equation of particle motion. In addition to the particle ions, a cold, incompressible ion fluid representing the plasmasphere is included in the inner magnetosphere. The electric field was calculated from the electron momentum equation, in which the electron flow velocity was derived from Ampere's law. The magnetic field was advanced in time using Faraday's law. Quasi-neutrality was assumed in the simulation. To simulate a foreshock bubble, we input a solar wind RD described by Rankine-Hugoniot relations.

The simulation used a spherical coordinate system (r, θ, ϕ) and was carried out within a geocentric distance of $4\,R_E < r < 25\,R_E$. The initial condition included a dipole geomagnetic field at $r < 10\,R_E$ (plus a mirror dipole field) and the solar wind at $r > 10\,R_E$. A solar wind RD was imposed to generate foreshock transients. The magnetic field of the solar wind with the RD was described by $B_x = -B_n = -B_{IMF} \cos \Delta\phi$, $B_y = -B_n \tan \phi$, $B_z = 0$, and $\phi = \Delta\phi \tanh[(x_{RD} - x)/w]$, where B_{IMF} is the magnitude of the interplanetary magnetic field (IMF), $B_n = B_{IMF} \cos \Delta\phi$ is the normal component of the IMF, x_{RD} is the x position of the RD's center, V_{RD} is the RD's propagation speed, and w is the RD's initial half-width. We chose $B_{IMF} = 5$ nT, $x_{RD0} = 50\,R_E$, $V_{RD} = 14V_A$ ($V_A = B_{IMF}/\sqrt{\mu_0 m_i N_0}$, where $N_0 = 6$ cm^{-3} is the solar wind density in this simulation; therefore, $V_A \simeq 44.5$ km/s), $w = 0.25\,R_E$, and $\Delta\phi = 20°$. The solar wind flow speed across the RD based on the Rankine-Hugoniot relations was $V_x = -V_{RD} - V_{An}$, $V_y = -V_{An} \tan \phi$, $V_z = 0$, where $V_{An} = V_A \cos \Delta\phi$.

About 4×10^8 particles were used in the simulation. Nonuniform grid spacing Δr was used to produce a higher resolution near the shock region, $\Delta r \simeq 1.0 d_i$, where $d_i = 0.1\,R_E$ is the scaled ion inertial length in the solar wind. A total grid of $160 \times 104 \times 130$ was used. The time step to advance the positions of ions was $\Delta t = 0.05 \Omega_i^{-1}$, where Ω_i is the unit ion gyrofrequency evaluated using $B = 10$ nT.

Betatron acceleration model

Because of the observed magnetic fluctuations with amplitude as large as the background field inside the core, electrons were isotropized there (fig. S2, C to F) (10). Scattering can lower the efficiency of betatron acceleration (but can also help keep electrons in the betatron acceleration region). If the scattering is faster than $\frac{dB}{dt}/B$, then it can cause $\langle E \rangle / B^{2/3}$ rather than $E_\perp / B$ to be constant (fig. S1), because $E_\parallel$, which does not increase through betatron acceleration, is averaged with $E_\perp$. The detailed derivation is shown below:

Betatron acceleration gives $\Delta E_\perp / E_\perp = \Delta B / B$. Scattering results in $\langle E \rangle = \frac{3}{2} E_\perp$, and energy increase does not change $\Delta \langle E \rangle = \Delta E_\perp$. Thus, we have $\Delta \langle E \rangle / \langle E \rangle = \frac{2}{3} \Delta B / B$ and $\langle E \rangle \sim B^{2/3}$.

In the FB sheath, where field strength is strong, the scattering effect is not fast enough to fully isotropize electrons. Therefore, we saw enhanced perpendicular anisotropy in the FB sheath: The PSD ratios of perpendicular to parallel and anti-parallel directions above tens of electron volts increased compared to the background [from black to blue/green in fig. S2 (C and D) and from blue to red in fig. S2 (E and F)], respectively.

REFERENCES AND NOTES

1. M. A. Lee, R. A. Mewaldt, J. Giacalone, Shock acceleration of ions in the heliosphere. *Space Sci. Rev.* **173**, 247–281 (2012).

2. E. A. Helder, J. Vink, A. M. Bykov, Y. Ohira, J. C. Raymond, R. Terrier, Observational signatures of particle acceleration in supernova remnants. *Space Sci. Rev.* **173**, 369–431 (2012).

3. C. S. Wu, A fast Fermi process: Energetic electrons accelerated by a nearly perpendicular bow shock. *J. Geophys. Res.* **89**, 8857–8862 (1984).

4. J. P. Eastwood, E. A. Lucek, C. Mazelle, K. Meziane, Y. Narita, J. Pickett, R. A. Treumann, The foreshock. *Space Sci. Rev.* **118**, 41–94 (2005).

5. A. Masters, L. Stawarz, M. Fujimoto, S. J. Schwartz, N. Sergis, M. F. Thomsen, A. Retinò, H. Hasegawa, B. Zieger, G. R. Lewis, A. J. Coates, P. Canu, M. K. Dougherty, Electron acceleration to relativistic energies at a strong quasi-parallel shock wave. *Nat. Phys.* **9**, 164–167 (2013).

6. L. B. Wilson III, D. G. Sibeck, D. L. Turner, A. Osmane, D. Caprioli, V. Angelopoulos, Relativistic electrons produced by foreshock disturbances observed upstream of Earth's bow shock. *Phys. Rev. Lett.* **117**, 215101 (2016).

7. R. A. Treumann, Fundamentals of collisionless shocks for astrophysical application, 1. Non-relativistic shocks. *Astron. Astrophys. Rev.* **17**, 409–535 (2009).

8. T. Z. Liu, H. Hietala, V. Angelopoulos, D. L. Turner, Observations of a new foreshock region upstream of a foreshock bubble's shock. *Geophys. Res. Lett.* **43**, 4708–4715 (2016).

9. T. Z. Liu, V. Angelopoulos, H. Hietala, L. B. Wilson III, Statistical study of particle acceleration in the core of foreshock transients. *J. Geophys. Res. Space Physics* **122**, 7197–7208 (2017).

10. T. Z. Liu, S. Lu, V. Angelopoulos, H. Hietala, L. B. Wilson III, Fermi acceleration of electrons inside foreshock transient cores. *J. Geophys. Res. Space Physics* **122**, 9248–9263 (2017).

11. T. Z. Liu, S. Lu, V. Angelopoulos, Y. Lin, X. Y. Wang, Ion acceleration inside foreshock transients. *J. Geophys. Res. Space Physics* **123**, 163–178 (2018).

12. D. L. Turner, L. B. Wilson III, T. Z. Liu, I. J. Cohen, S. J. Schwartz, A. Osmane, J. F. Fennell, J. H. Clemmons, J. B. Blake, J. Westlake, B. H. Mauk, A. N. Jaynes, T. Leonard, D. N. Baker, R. J. Strangeway, C. T. Russell, D. J. Gershman, L. Avanov, B. L. Giles, R. B. Torbert, J. Broll, R. G. Gomez, S. A. Fuselier, J. L. Burch, Autogenous and efficient acceleration of energetic ions upstream of Earth's bow shock. *Nature* **561**, 206–210 (2018).

13. N. Omidi, J. P. Eastwood, D. G. Sibeck, Foreshock bubbles and their global magnetospheric impacts. *J. Geophys. Res.* **115**, A06204 (2010).

14. D. L. Turner, N. Omidi, D. G. Sibeck, V. Angelopoulos, First observations of foreshock bubbles upstream of Earth's bow shock: Characteristics and comparisons to HFAs. *J. Geophys. Res. Space Physics* **118**, 1552–1570 (2013).

15. T. Z. Liu, D. L. Turner, V. Angelopoulos, N. Omidi, Multipoint observations of the structure and evolution of foreshock bubbles and their relation to hot flow anomalies. *J. Geophys. Res. Space Physics* **121**, 5489–5509 (2016).

16. V. Angelopoulos, The THEMIS mission. *Space Sci. Rev.* **141**, 5–34 (2008).

17. J. P. McFadden, C. W. Carlson, D. Larson, M. Ludlam, R. Abiad, B. Elliott, P. Turin, M. Marckwordt, V. Angelopoulos, The THEMIS ESA plasma instrument and in-flight calibration. *Space Sci. Rev.* **141**, 277–302 (2008).

18. H. U. Auster, K. H. Glassmeier, W. Magnes, O. Aydogar, W. Baumjohann, D. Constantinescu, D. Fischer, K. H. Fornacon, E. Georgescu, P. Harvey, O. Hillenmaier, R. Kroth, M. Ludlam, Y. Narita, R. Nakamura, K. Okrafka, F. Plaschke, I. Richter, H. Schwarzl, B. Stoll, A. Valavanoglou, M. Wiedemann, The THEMIS fluxgate magnetometer. *Space Sci. Rev.* **141**, 235–264 (2008).

19. Y. Lin, X. Y. Wang, Three-dimensional global hybrid simulation of dayside dynamics associated with the quasi-parallel bow shock. *J. Geophys. Res.* **110**, A12216 (2005).

Citation: T. Z. Liu, V. Angelopoulos, S. Lu, Relativistic electrons generated at Earth's quasi-parallel bow shock. *Sci. Adv.* **5**, eaaw1368 (2019).